Article

Study on the Low-Frequency and Broadband Sound Absorption Performance of an Underwater Anechoic Layer with Novel Design

Jinshun Hu [1], Yongshui Lin [1,*], Zhiwei Zhou [2,*], Xiaofei Cao [1], Qingjia Chi [1] and Weiguo Wu [3]

[1]   School of Science, Wuhan University of Technology, Wuhan 430070, China
[2]   Beijing Key Laboratory of Lightweight Multi-Functional Composite Materials and Structures,
     Institute of Advanced Structure Technology, Beijing Institute of Technology, Beijing 100081, China
[3]   Green & Smart River-Sea-Going Ship, Cruise and Yacht Research Center, Wuhan University of Technology,
     Wuhan 430063W, China
*   Correspondence: linyongshui1226@whut.edu.cn (Y.L.); zhouzw92@bit.edu.cn (Z.Z.)

Abstract: To further improve the low-frequency broadband sound absorption capability of the underwater anechoic layer (UAL) on the surface of marine equipment, a novel sound absorption structure with cavities (NSSC) is designed by adding resonators and honeycombs to the traditional sound absorption structure with cavities (SSC). Based on the principle of shear dissipation, the original intention of the design is to allow more parts of the viscoelastic material to participate the dissipation of acoustic energy. The approximate multilayer sound absorption theoretical model based on the modified transfer matrix method is used to verify the accuracy of finite element calculations. In the frequency range of 1100 Hz–10,000 Hz, the sound absorption coefficient (α) of NSSC can reach 0.8. The effects of the presence and size of cylindrical oscillators and honeycomb structures on sound absorption are discussed in detail. The results show that expanding the effective sound absorption range of the damping area of the structure is the key to improve the wideband sound absorption effect. This design concept could guide the structural design of the UAL.

Keywords: low-frequency broadband sound absorption; air cavity; cylindrical oscillator; honeycomb

1. Introduction

UALs are generally used to cover the surface of an underwater vehicle to counteract the active or passive sonar detection [1–4]. Its stealth performance for submarines and other underwater vehicles is crucial and has been widely valued by various maritime military powers. The UALs with good sound absorption performance should satisfy both important principles [5]: (1) the acoustic material is consistent with the characteristic impedance of the water as much as possible, so that the sound waves can fully enter the anechoic material and the corresponding reflection is reduced; (2) the anechoic material has a high sound wave absorption capacity. Viscoelastic materials such as rubber meet the above requirements and are widely employed for underwater sound absorption [6–13].

UALs require high sound absorption capabilities at a wide frequency band, but most homogeneous materials often fall short of the requirement. To overcome the limitation, researchers proposed the polymer mixed sound absorbing materials [14], polymer foam sound absorbing materials [15], gradient sound absorbing materials [16], and filled sound absorbing materials [17]. Among them, the more mature studies of UALs mainly focus on composite structures with cavities or resonators [18].

Viscoelastic materials with cavities can absorb more energy under sound wave incidence owing to the principle of shear dissipation and the resonance of cavities [19,20]. Ivansson et al. [21] compared the sound absorption properties of an attenuated coating containing cylindrical holes with different cross-sectional shapes (circular, oval, and super-ellipse) and obtained the optimal solution using the Markov chain Monte Carlo method.

Ye et al. [22] studied the effects of different shapes of cavities and found that the horn holes have the best sound absorption performance at lower frequencies. These cavity structures are often called Alberich anechoic materials [23]. The backing material also significantly impacts the sound absorption of Alberich anechoic materials. Alberich anechoic materials are usually soaked in steel-backed water. Zhao et al. [24] studied the optimization and mechanism of Alberich anechoic materials on steel plates. It is found that laying different coatings on the two surfaces of the steel plate can effectively improve the low-frequency sound absorption and the sound absorption bandwidth. Locally resonant structures usually consist of a heavy core and soft viscoelastic material. Near the resonant frequency, the vibrations of the structure enhance the friction between the molecules, then the dissipation of sound energy rises. Gao et al. [25] introduced a broadband sound absorbing underwater metamaterial composed of viscoelastic rubber, conical cavities, cylindrical oscillators, and backing steel. Compared with pure viscoelastic rubber and traditional sound absorbing structures with cavities, the structure exhibits excellent broadband sound absorption performance below 10 kHz. Jin et al. [26] proposed a novel composite acoustic metamaterial made of periodic multi-resonators and cavities. Numerical calculations show that the coupled resonance generated by multiple resonators and cavities can effectively broaden the sound absorption frequency band. In addition, previous works have not discussed the sound absorption valley in the mid-high frequency of UALs with cavities. Compared with pure viscoelastic material, the appearance of the cavities makes UAL appear at the sound absorption peak at low frequency. Nevertheless, the α cannot maintain a high value in the subsequent mid-to-high frequency bands [7,25–30].

In this paper, NSSC is proposed to improve the low-frequency and broadband sound absorption capability of UAL. Compared with SSC, cylindrical oscillators and periodic hexagonal steel honeycomb are added. The theoretical calculation verifies the correctness of the finite element method. The validated finite element model is then used to explore the sound absorption characteristic of the new structure and to quantify the geometry dependence of the sound absorption.

For the first time, the structure of UAL (NSSC) proposed in this paper combines the viscoelastic material, cavities, cylindrical oscillator, and steel honeycomb to achieve low-frequency broadband sound absorption. Among them, the cavity plays a role in improving overall sound absorption. The cylindrical oscillators significantly rise the low-frequency sound absorption. The honeycomb enhances the dissipation of sound energy in most of the damping area of UAL, improves the sound absorption of mid- and high-frequency, and eliminates the sound absorption valley.

2. Methods

2.1. Geometric Model and Material

As displayed in Figure 1, the lateral dimension of the UAL is assumed to be infinite and consisted of a periodic arrangement of hexagonal cells. To facilitate the theoretical verification, the hexagonal prism is approximated as a cylinder based on the principle that the volume fraction of the cavity in the cell remains unchanged. This approximation has been proven to be sufficiently accurate [31]. The geometric parameters and material parameters of the UAL are listed in Tables 1 and 2. l_1 is the height from the top of the UAL to the cavity, l_2 is the height of the cavity, r_1 is the radius of the cavity, r_2 is the cell radius, r_3 is the radius of the cylinder, t is the half of thickness of the honeycomb, h_1 is the height of the honeycomb, h_2 is the height from the bottom of the cylinder to the backing steel, h_3 is the height of the cylinder.

Table 1. The geometric parameters of the UAL (mm).

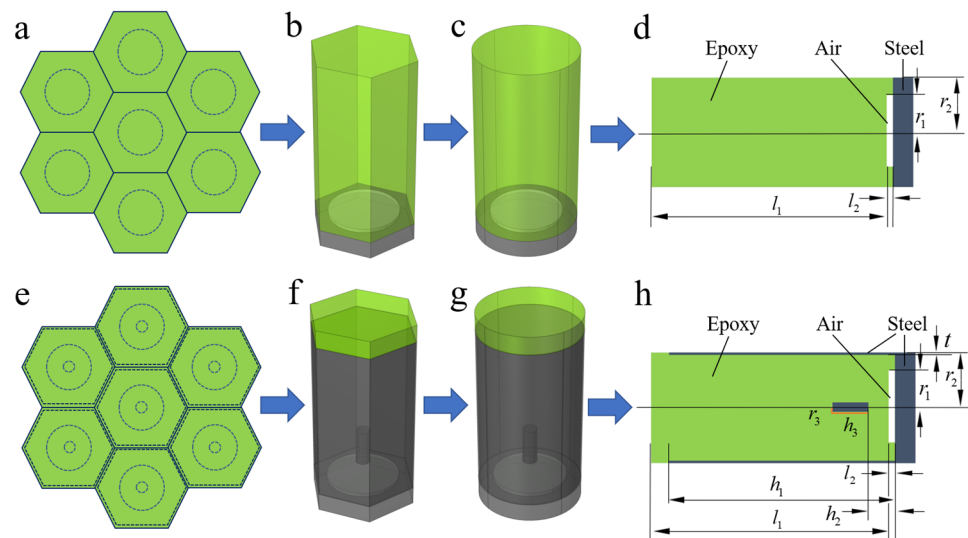| l_1	l_2	r_1	r_2	r_3	t	h_1	h_2	h_3
49	1	10	15	2	0.5	45	5	10

Figure 1. (**a**–**d**) are the top view, hexagonal cell, cylindrical cell, and cross-sectional of SSC; (**e**–**h**) are the top view, hexagonal cell, cylindrical cell and cross-sectional of NSSC.

Table 2. Material parameters "Adapted with permission from Ref. [26]. 2020, Elsevier Ltd.".

Solid Medium	Density (kg/m³)	Elastic Modulus (GPa)	Poisson's Ratio	Loss Factor
Epoxy	1100	0.027	0.49	0.6
Steel	7980	210	0.28	/

2.2. Theoretical α of SSC

The α of SSC was theoretically calculated via the transfer matrix method. Figure 2 exhibits the working condition of a typical cell. The transverse dimension of the UAL is infinite. The vertically incident plane sound wave from the water passes through the UAL and reaches the back steel plate which could be regarded as the hard boundary. Then, the sound wave is reflected to the UAL and eventually back into the water.
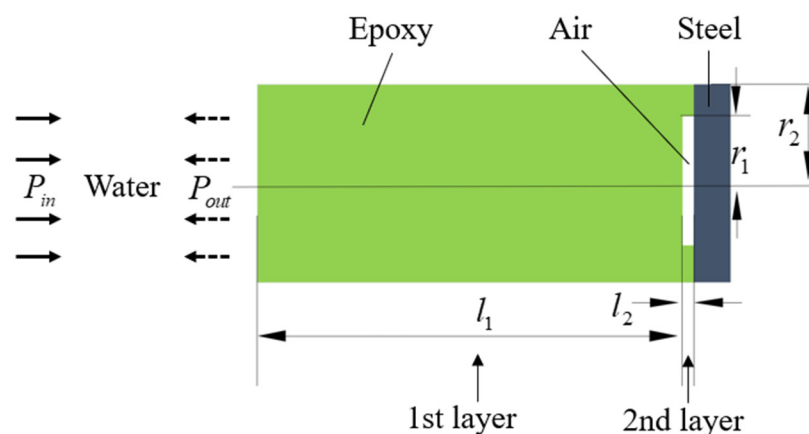

Figure 2. Structural parameters and working conditions of typical cell of SSC.

The SSC is divided into two layers. The first layer is a uniform viscoelastic material, and the sound velocity [27] is

$$c_1 = \sqrt{\frac{E_1(1-v)}{\rho_1(1+v)(1-2v)}} \tag{1}$$

$$E_1 = E_s(1 + \mathrm{j}\eta) \tag{2}$$

where E_1 and ρ_1 are the complex elastic modulus and density of the first layer, v and η are the Poisson's ratio and loss factor of the viscoelastic material. E_s is the elastic modulus and j is the imaginary unit. The complex wavenumber of the first layer is

$$k_1 = \omega / c_1 \tag{3}$$

in which $\omega = 2\pi f$ is the circular frequency, f is the frequency.

The second layer is a viscoelastic material with a cavity, and its approximate complex wavenumber [27] is expressed as

$$k_2 = k_1 \sqrt{1 + \frac{\lambda}{\mu} \frac{\varepsilon^2}{1 - \varepsilon^2}} \tag{4}$$

with

$$\lambda = \frac{v E_1}{(1 + v)(1 - 2v)} \tag{5}$$

$$\mu = \frac{E_1}{2(1 + v)} \tag{6}$$

$$\varepsilon = r_1 / r_2 \tag{7}$$

where λ and μ are the Lame coefficients of t/he viscoelastic material, and ε is the ratio of the inner diameter to the outer diameter of the second layer. Due to the existence of the cavity, the equivalent density of the second layer is

$$\rho_2 = \rho_a \varepsilon^2 + \rho_1 \left(1 - \varepsilon^2\right) \tag{8}$$

in which ρ_a is the air density.

The sound velocity of the second layer is

$$c_2 = \omega / k_2 \tag{9}$$

For a multi-layer structure, the transfer matrix of the i-th layer is written as

$$\mathbf{T_i} = \begin{bmatrix} \cos(k_i l_i) & \mathrm{j}\rho_i c_i \sin(k_i l_i) \\ \mathrm{j}\sin(k_i l_i)/\rho_i c_i & \cos(k_i l_i) \end{bmatrix} \tag{10}$$

where k_i is the complex wavenumber of the i-th layer, l_i is the thickness of the i-th layer, ρ_i is the equivalent density of the i-th layer, and c_i is the sound velocity of the i-th layer. Previous studies [32] have shown that the low-frequency sound absorption performance in such cylindrical pipes is mainly affected by the first axisymmetric wavenumber associated with the first propagation mode. Therefore, only the first wavenumber k_i is considered here, and the transfer matrix formula of Equation (10) can be used. In this paper, the low-frequency range (less than 10 kHz) is considered, in which the acoustic wave wavelength far exceeds the thickness of the anechoic layer, so the transfer matrix method is appropriate.

The total transmission matrix of the anechoic layer is the successive multiplication of the transmission matrix of each layer as

$$\mathbf{T} = \begin{bmatrix} T_{11} & T_{12} \\ T_{21} & T_{22} \end{bmatrix} = \prod_{i=1}^{n} \mathbf{T_i} \tag{11}$$

According to the transfer function method, the sound pressure and vibration velocity of the front interface and the rear interface can be related by **T** as

$$\begin{bmatrix} \rho_1 \\ v_1 \end{bmatrix} = \mathbf{T} \begin{bmatrix} T_{11} & T_{12} \\ T_{21} & T_{22} \end{bmatrix} \begin{bmatrix} \rho_2 \\ v_2 \end{bmatrix} \tag{12}$$

in which ρ_1 and v_1 are the sound pressure and vibration velocity of the front interface, ρ_2 and v_2 are the sound pressure and vibration velocity of the rear interface.

The impedances of the front and rear interfaces are equal to their corresponding sound pressure, expressed as

$$Z_1 = \rho_1/v_1 \tag{13}$$

$$Z_2 = \rho_2/v_2 \tag{14}$$

When the interface impedance tends to infinity at the rigid backing, there is

$$Z_1 = T_{11}/T_{21} \tag{15}$$

The reflection coefficient of the anechoic layer is

$$R = (Z_1 - Z_w)/(Z_1 - Z_w) \tag{16}$$

where Z_w is the impedance of the aqueous medium.

Finally, the α can be achieved as

$$\alpha = 1 - |R|^2 \tag{17}$$

2.3. Verification of Finite Element Analysis

The two-dimensional axisymmetric model in the finite element software COMSOL can perfectly fit the periodicity and symmetry of the sound absorbing layer [33,34]. As shown in Figure 3, the finite element model from left to right is the perfect matching layer, the water, and the sound absorbing layer. The perfectly matched layer absorbs all sound waves and simulates an infinite acoustic domain. A background pressure field is added to the water to simulate the plane wave incidence. The radial displacement of the outer boundary of the cylinder is 0. The quadratic Lagrange element was used in the acoustic domain and the quadratic serendipity element was used in the solid domain. The mesh size is set to 1 mm to meet the calculation accuracy. The total number of elements is 1275.
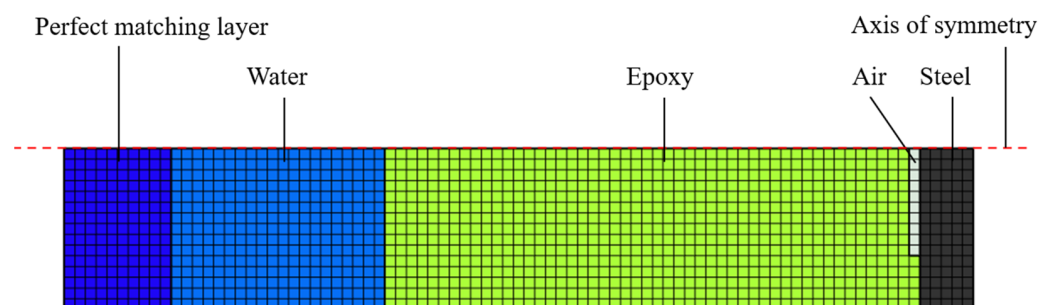

Figure 3. Finite element model of UAL of SSC.

The theoretical and the simulated α of SSC are presented in Figure 4. In the considered frequency range from 0 Hz to 10,000 Hz with the step 10 Hz, the results are in good agreement with each other. Thus, the correctness of the finite element model of the UAL is confirmed. The slight discrepancies in the α observed in the figure are a result of the approximate complex wavenumber in Equation (4).
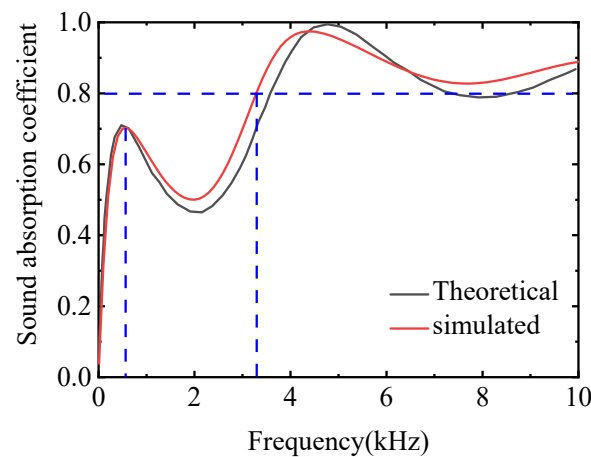
Figure 4. Comparison of α between SSC theoretical model and finite element model.

3. Acoustic Absorption Mechanism

In this paper, 0.8 is a reference value for the high α. Figure 4 shows that the SSC can achieve high sound absorption within 3300–10,000 Hz. However, the SSC also has a sound absorption valley in the mid-frequency region (around 2000 Hz), which exists widely in the work of some other researchers [7,25–30]. To improve the low-frequency and broadband sound absorption capability, a cylindrical oscillator is added and the SSC-CO (sound absorption structure with cavities and cylindrical oscillators) is formed. A periodic hexagonal steel honeycomb is added to obtain SSC-HSH (sound absorption structure with cavities and hexagonal steel honeycomb). Finally, both the cylindrical oscillator and a periodic steel honeycomb are added and the design of NSSC is gained. All structures are displayed in Figure 5.
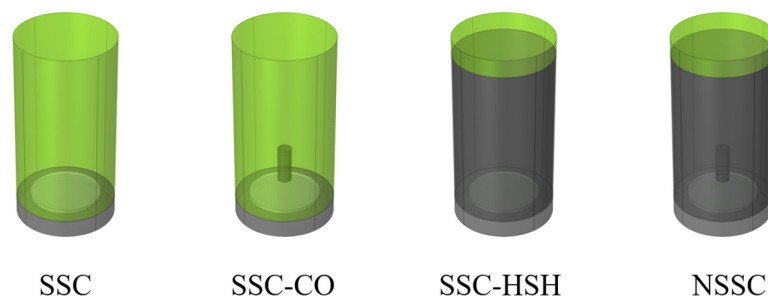

Figure 5. Sound absorption structure with cavities (SSC) and its derivatives (SSC-CO, SSC-HSH, NSSC).

3.1. The Sound Absorption Appearance of Each UAL

The comparison of the α of the above four structures is given in Figure 6. According to the trend of the α curves, it can be divided into two categories for discussion. The α curves of SSC and SSC-CO begin to decline after reaching the first absorption peak at 600 Hz and the valley of sound absorption around 2000 Hz, and then the sound absorption curve rises again. However, the α curves of SSC-HSH and NSSC have no sound absorption valley near 2000 Hz and show continuously rising trends. The NSSC has the best sound absorption ability and can achieve wide-band high sound absorption at 2000–10,000 Hz.

To further understand the sound absorption mechanism of the underwater UAL proposed in this paper, the total displacement nephogram (Figure 7) and the radial velocity nephogram (Figure 8) at 600 Hz, 2000 Hz, and 4000 Hz are selected for comparative analyses. The SSC and SSC-CO, SSC-HSH, and NSSC, respectively, have similar displacement and radial velocity distribution. This phenomenon explains that the NSSC and SSC-CO, SSC-HSH, and NSSC have similar sound absorption curves in Figure 6.
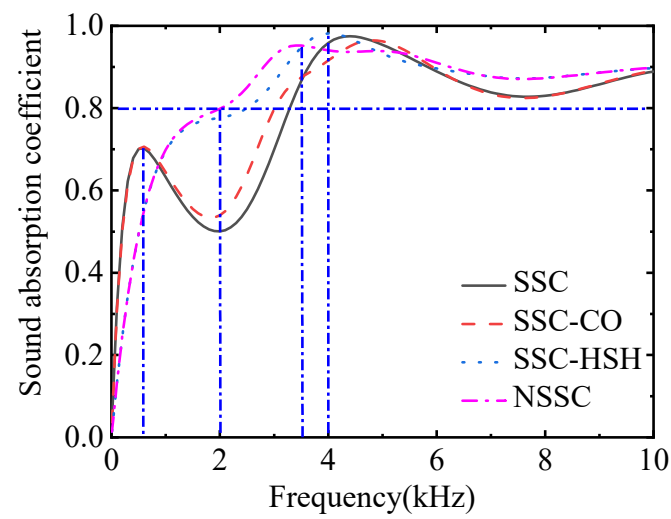
Figure 6. Comparison of α of SSC, SSC-CO, SSC-HSH, and NSSC.
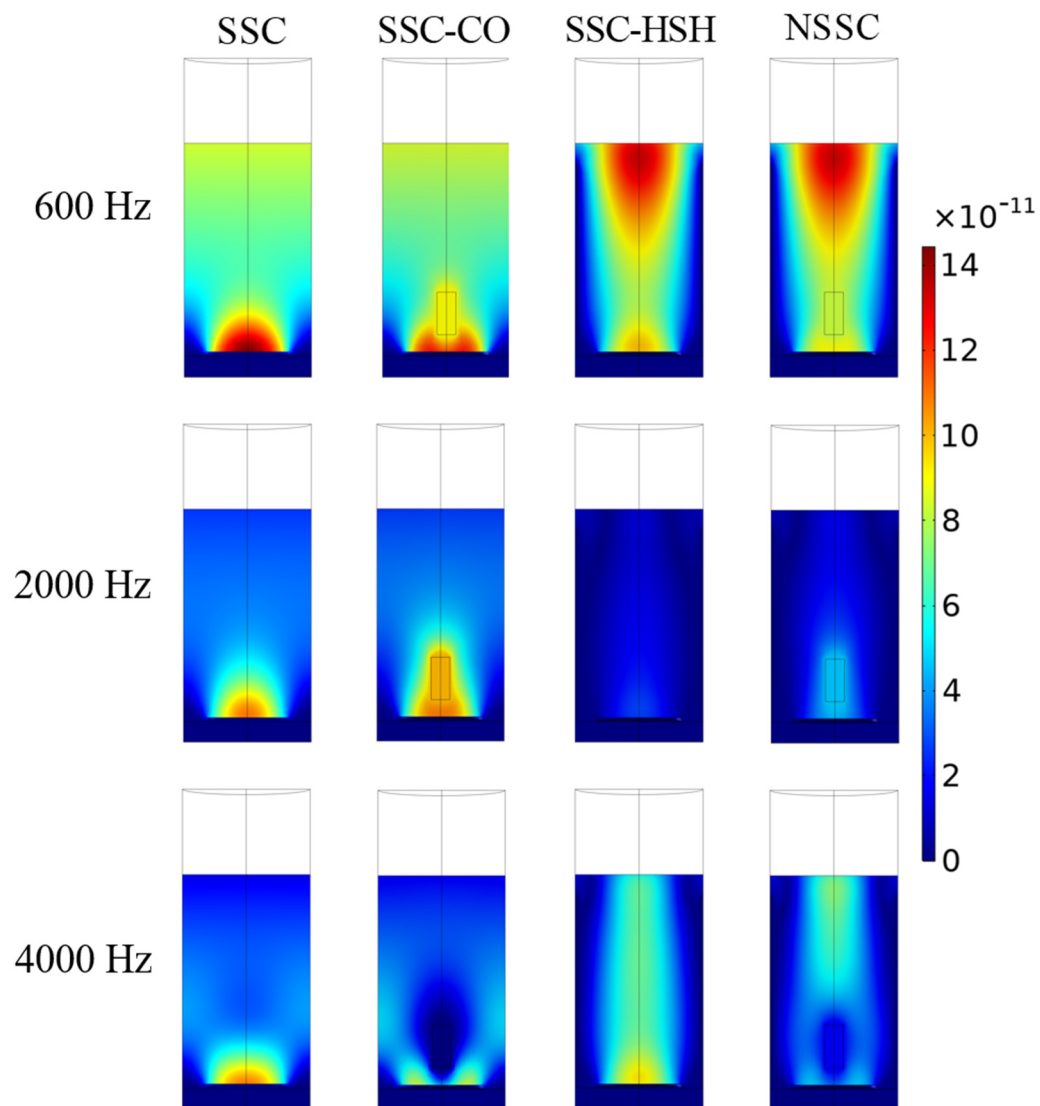

Figure 7. Displacement nephogram of each configuration (unit: m).

In Figure 7, when the UAL has no honeycomb (SSC and SSC-CO), the displacement of the damping region is relatively uniform from top to bottom, and its displacement along the radial direction is not obvious until it is close to the cavity or cylinder. When the incident wave frequency increases from 600 Hz to 2000 Hz and then to 4000 Hz, the total displacement of UAL decreases significantly. There is no displacement in the damping area near the honeycomb after the addition of honeycombs (SSC-HSH and NSSC). The displacement of UAL changes notably along the radial direction. The honeycomb weakens the displacement of the UAL. When the incident wave frequency increased from 600 Hz to 2000 Hz and then to 4000 Hz, the total displacement of UAL showed a trend of first decreasing and then increasing.
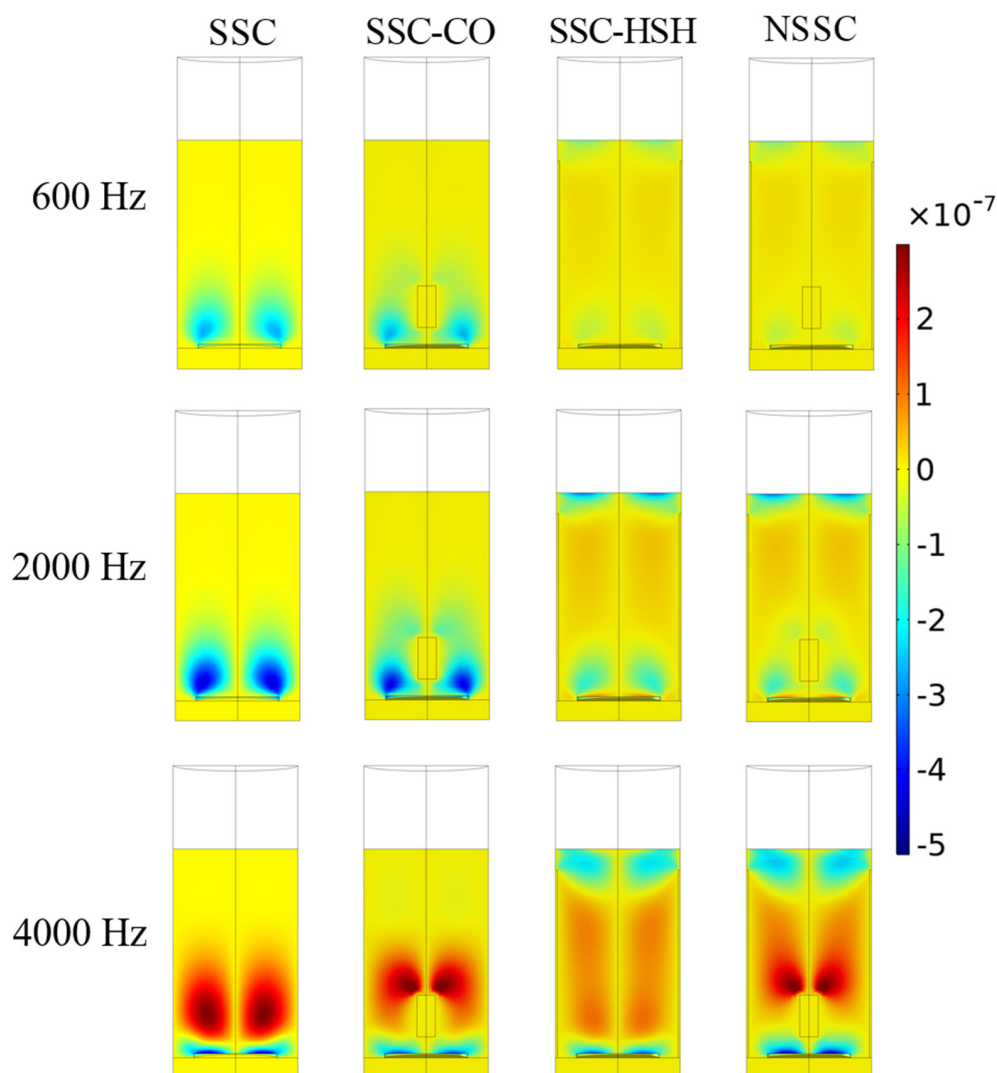

Figure 8. Radial velocity nephogram of each configuration (unit: m/s).

In Figure 8, when the UAL has no honeycomb (SSC and SSC-CO), its radial velocity is concentrated at the outer edge of the cavity, and the radial velocity is not observed in the middle and upper parts of the UAL. This is due to the nonlinear vibration of the damping area near the cavity, and the damping area in the upper middle is relatively static in the radial direction. When a honeycomb is added (SSC-HSH and NSSC), the radial velocity exists throughout the UAL due to the mutual shearing motion of the honeycomb and damping areas. Furthermore, the resonant cylinder suppresses the radial velocity of the surrounding damping region. When the incident wave frequency increases from 600 Hz to 2000 Hz and then to 4000 Hz, the radial velocity increases with the growth in frequency.

3.2. The Relationship between the Curves and the Nephograms

The radial velocity reflects the shear wave propagation. In viscoelastic media, shear waves dissipate the acoustic energy much more strongly than longitudinal waves. In Figure 8, the radial velocity of UAL is proportional to the frequency. It explains that the α of SSC-HSH and NSSC continue to rise at 600–4000 Hz. However, due to the large overall displacements of SSC and SSC-CO at 600 Hz (as shown in Figure 7), a large amount of energy is dissipated and the first sound absorption peak in the sound absorption curve is caused. At 600–4000 Hz, it shows a trend of first decreasing and then increasing. The honeycomb limits the overall displacement of SSC-HSH and NSSC at 600 Hz, which explains that the α of SSC-HSH and NSSC at 600 Hz is smaller than that of SSC and SSC-CO, and the sound absorption curve cannot reflect the first absorption peak. Compared with SSC and SSC-CO, the radial velocity distributions of SSC-HSH and NSSC are wider, and there are more parts for efficient energy dissipations of UAL. Thus, with the increase in frequency, the α of SSC-HSH and NSSC exceeds that of SSC and SSC-CO. The cylinder insertion is designed based on the contribution of the local resonant resonators to the acoustic low-frequency absorption. Consequently, before 3500 Hz, the α of UAL with the cylindrical oscillator is greater than that of UAL without the resonator cylinder (SSC-CO > SSC, NSSC > SSC-CO), but at 4000 Hz the situation is slightly opposite (SSC-CO < SSC, NSSC < SSC-CO). This can still be explained by Figures 7 and 8. At low frequencies (600 Hz), the sound absorption of the anechoic layer is determined by the overall displacement. The influence of the resonant body can be ignored, making the sound absorption curve the same. As the frequency increases, for example, when the frequency is 2000 Hz, the overall displacement of the UAL decreases, and the area near the cylindrical oscillator contributes part of the displacement and radial velocity, which makes the α of the UAL with the cylindrical oscillator larger. When the frequency increases to 4000 Hz, the region near the resonator suppresses part of the displacement and radial velocity so that the α of the UAL with the cylindrical oscillator is small.

In summary, improving the area size of structural sound energy dissipation is the key to improving the α. It is necessary to further study the influence of the size of the cylinder and honeycomb on the α.

4. The Influence of Different Parameters on the α

4.1. Influence of the Honeycomb Size on α

The analysis of the sound absorption reveals that the honeycomb confines the SSC-HSH in a vertical direction, reducing the overall displacement of the SSC-HSH. Still, the part of the SSC-HSH that can dissipate energy efficiently becomes more. Figure 9 further shows the α of the SSC-HSH under different honeycomb heights. With the increase in the height of the honeycomb, the larger the structural restraint range, the smaller the total displacement of the SSC-HSH at low frequencies (less than 600 Hz), and the correspondingly smaller α. However, at around 2000 Hz, with the increase in the height of the honeycomb, more parts of the SSC-HSH efficiently dissipate energy, and the sound absorption valley in the curve becomes smaller and smaller until it disappears. From 0 to 4000 Hz, the overall performance is that with the increase in the height of the honeycomb, the α first decreases and then increases. However, the low-frequency sacrifice is acceptable because it makes up for the defect of the valley in the α at around 2000 Hz.

Figure 10 shows the corresponding α for different honeycomb thicknesses. Changes in thickness do not substantially change the size of the energy dissipation area in SSC-HSH, which has similar α at each thickness. As the honeycomb thickness increases, the viscoelastic region of the SSC-HSH becomes more constrained. Before 1250 Hz, the larger the thickness, the smaller the α; after 1250 Hz, the larger the thickness, the larger the α. Therefore, the height of the honeycomb is the main factor affecting the α of SSC-HSH. Additionally, the sound absorption performance of SSC-HSH is proportional to the height of the honeycomb.
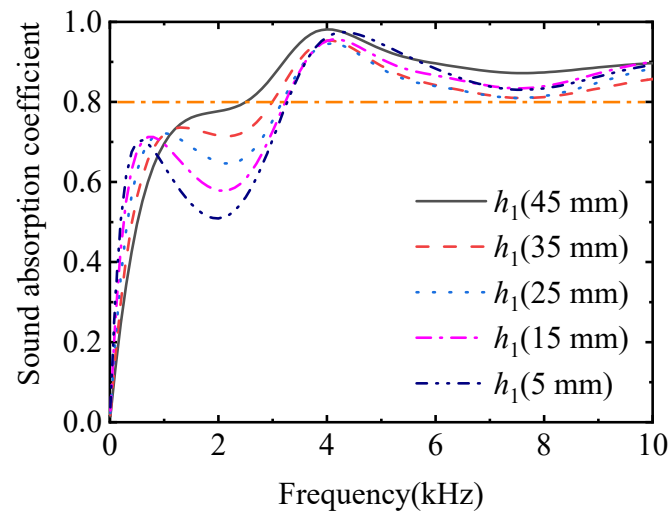
Figure 9. Comparison of α of SSC-HSH corresponding to different honeycomb heights.
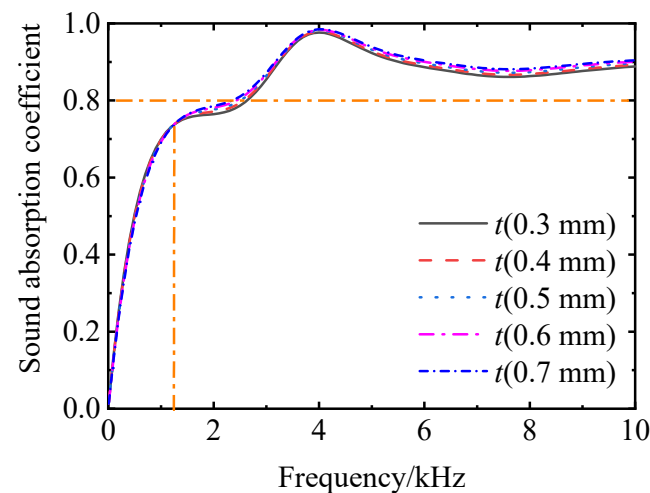

Figure 10. Comparison of α of SSC-HSH corresponding to different honeycomb thicknesses.

4.2. Influence of the Cylinder Size on α

Based on the local resonant resonator principle, the cylinder is inserted into the structure to enhance its low-frequency sound absorption. Figure 11 shows the α of SSC-CO corresponding to different cylinder radii. The radius of the cylinder has a significant effect on the sound absorption effect of SSC-CO. When the radius increases from 2 mm to 6 mm, the frequency of the sound absorption curve reaching 0.8 for the first time keeps moving to the low frequency; when the radius increases from 6 mm to 10 mm, the frequency of the sound absorption curve reaching 0.8 for the first time did not move to the low frequency significantly, and even at 10mm, the frequency reaching 0.8 for the first time moved to the high frequency instead. In addition, at around 4000 Hz, the α of SSC-CO with 8 mm and 10 mm cylinder radii dropped below 0.8. The appearance of this is due to the joint coupling between the cylinder and the bottom cavity. From the analysis of the sound absorption mechanism in Section 3.2, the displacement and radial velocity near the cavity mainly exist outside the cavity radius. When the radius of the cylinder is 10 mm, the cylinder suppresses the displacement and vibration of the viscoelastic material near the cavity and reduces the sound energy dissipation.
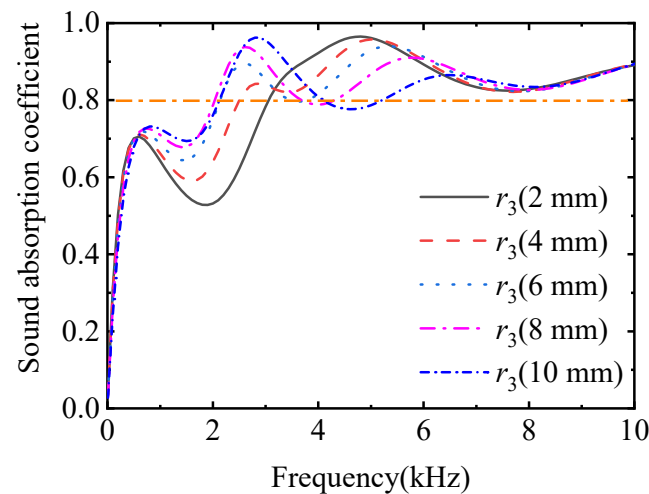
Figure 11. Comparison of α of SSC-CO corresponding to different cylinder radii.

Figure 12 shows the α of SSC-CO corresponding to different cylinder heights. Section 3.2 points out that the displacement of the viscoelastic region in the upper part of the cylinder is relatively uniform, and there is no radial velocity, so the increase in height does not significantly change the sound absorption performance of the SSC-CO. Therefore, the radius of the cylinder is the main factor affecting the α of the SSC-CO. The selection of the radius needs to consider the coupling with the cavity. In SSC-CO, the sound absorption effect is best when the radius is around 6 mm.
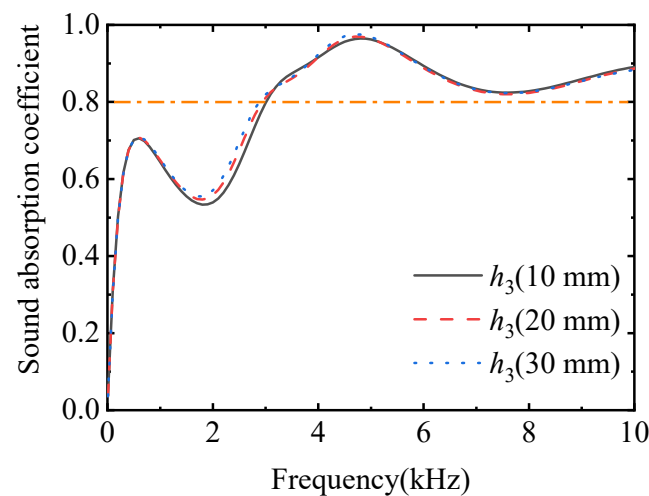

Figure 12. Comparison of α of SSC-CO corresponding to different cylinder heights.

4.3. The Effect of the Joint Action of the Honeycomb and the Cylinder on the α

In this section, the honeycomb and the cylinder are considered together to explore the impact on the sound absorption performance of NSSC. To maximize the restraint range of the honeycomb on NSSC and ensure the smoothness of the outer surface of UAL, the height of the honeycomb $h_1 = 49$ mm, and the other geometric parameters are consistent with Table 1. The influence on the α of NSSC is obtained by changing the radius of the cylinder and the height of the cylinder, respectively.

In Figure 13, as the radius of the cylinder increases, the frequency when the curve first reaches 0.8 moves to low frequencies. However, when the radius is 10 mm, the frequency at which the curve first comes 0.8 moves to the high frequency instead. This is exactly in line with the trend in Section 4.2. Due to the addition of the honeycomb, the overall sound absorption performance of NSSC has been improved to a certain extent, so there is no frequency band with a α lower than 0.8 in the follow-up. In Figure 14, the change

in the cylinder height has a great influence on the sound absorption of the NSSC (refer to Section 4.2, the cylinder radius is taken as 6 mm). Unlike SSC-CO, due to the presence of the honeycomb, the damping area performs shear motion with both the honeycomb and the cylinder to dissipate more sound energy. It is shown that the higher the cylinder, the better the sound absorption capacity of NSSC.
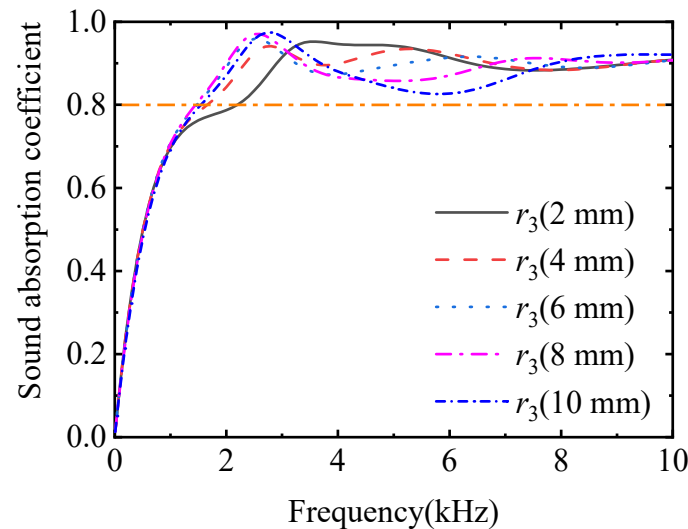

Figure 13. Comparison of α of NSSC corresponding to different cylinder radii.
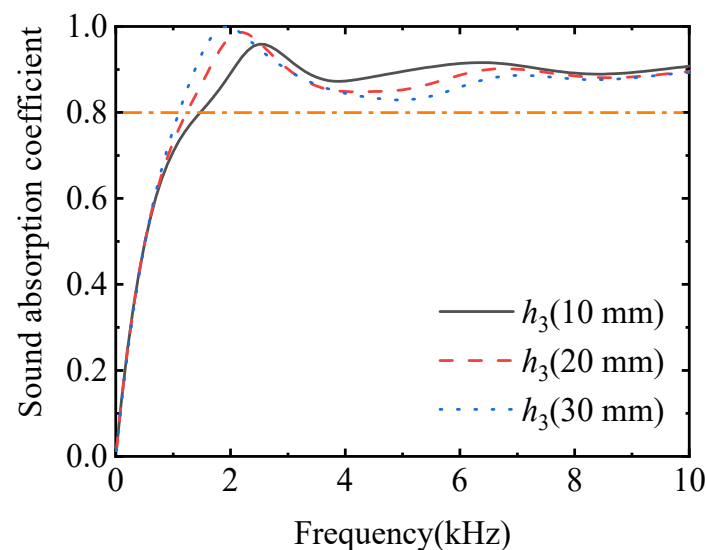

Figure 14. Comparison of α of NSSC corresponding to different cylinder heights.

4.4. Comparison with Typical UALs

For sonar detection below 10,000 Hz, it is difficult for most of the underwater anechoic layer to meet the low-frequency broadband α of 0.8 and above. To demonstrate the effectiveness of the combined structure of cavity, resonant cylinder, and honeycomb, the effective sound absorption bandwidth ($\alpha > 0.8$) of NSSC is compared with the previous typical UAL (Refs. [27,28]) in Figure 15. The comparison shows that NSSC can achieve effective sound absorption in the frequency range of (1100–10,000) Hz, with the largest sound absorption bandwidth.
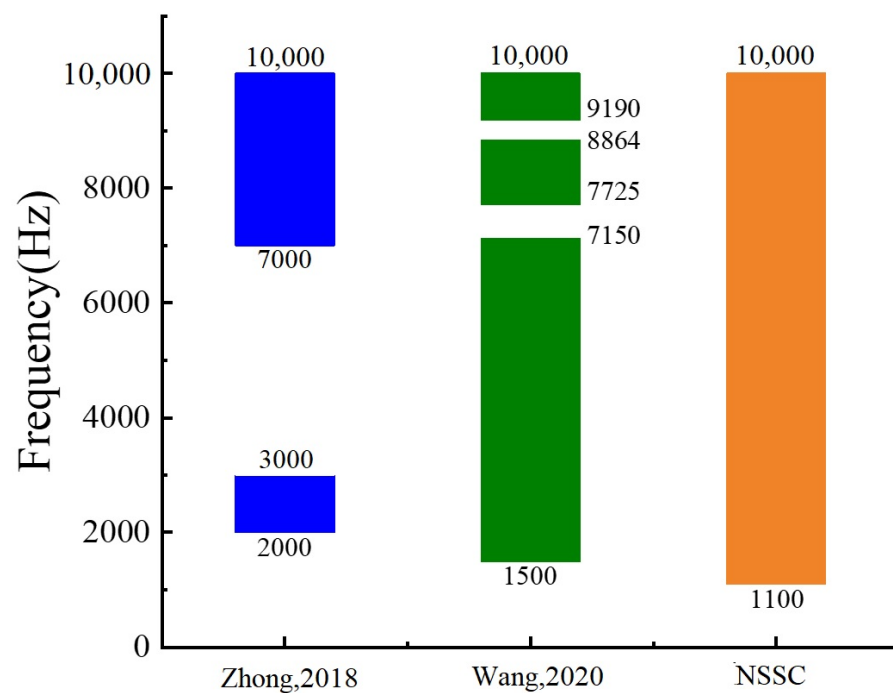
Figure 15. Comparison of absorption bandwidths with absorption coefficients above 0.8 between NSSC and other UALs in representative references [27,28].

5. Conclusions

A new type of underwater sound absorbing structure consisting of viscoelastic material, cavities, cylindrical oscillator, steel honeycomb, and backing steel was designed. The theoretical sound absorption coefficient was well matched with the simulated sound absorption coefficient, validating the reliability of the calculation. In addition, the geometry dependence of the underwater sound absorption performance of NSSC (novel sound absorption structure with cavities) was studied. The design would significantly increase the acoustic energy consumption of the structure as seen from the principle of shear dissipation. By adding honeycomb, the sound absorption valley could be effectively compensated, and the sound absorption capacity of med- and high-frequency of the underwater anechoic layer could be significantly improved. The sound absorption performance was improved as the honeycomb height increased. The low-frequency acoustic absorption capacity of the structure was improved by the addition of cylindrical oscillators. The choice of cylindrical radius and height should be determined based on the cavity radius and honeycomb height. Compared with other underwater sound absorption structures, the sound absorption coefficient of NSSC can reach 0.8 in the 1100–10,000 Hz frequency band, which has obvious low-frequency wideband sound absorption advantages. This design concept could guide the structural design of the underwater anechoic layer in the future.

References

1. Ke, Y.; Zhang, L.; Zhao, X.; Tao, M. An equivalent method for predicting acoustic scattering of coated shell using identified viscoelastic parameters of anechoic coating. *Appl. Acoust.* **2021**, *179*, 108071. [CrossRef]
2. Zhang, Z.; Huang, Y.; Huang, Q. Low-frequency broadband absorption of underwater composite anechoic coating with periodic subwavelength arrays of shunted piezoelectric patches. *Compos. Struct.* **2019**, *216*, 449–463. [CrossRef]
3. Meng, H.; Wen, J.; Zhao, H.; Wen, X. Optimization of locally resonant acoustic metamaterials on underwater sound absorption characteristics. *J. Sound Vib.* **2012**, *331*, 4406–4416. [CrossRef]
4. Zhang, Z.; Li, Z.; Li, T.; Huang, Q. A novel semi-analytical approach for predicting the sound absorptions of a new underwater composite coating with transversely arranged SWCNTs. *Compos. Struct.* **2021**, *274*, 114335. [CrossRef]
5. Ross, C.T.F. A conceptual design of an underwater vehicle. *Ocean Eng.* **2006**, *33*, 2087–2104. [CrossRef]
6. Zhang, Y.; Cheng, L. Ultra-thin and broadband low-frequency underwater acoustic meta-absorber. *Int. J. Mech. Sci.* **2021**, *210*, 106732. [CrossRef]
7. Sharma, G.S.; Skvortsov, A.; MacGillivray, I.; Kessissoglou, N. Sound absorption by rubber coatings with periodic voids and hard inclusions. *Appl. Acoust.* **2019**, *143*, 200–210. [CrossRef]
8. Yu, T.; Jiang, F.; Wang, J.; Wang, Z.; Chang, Y.; Guo, C. Acoustic insulation and absorption mechanism of metallic hollow spheres composites with different polymer matrix. *Compos. Struct.* **2020**, *248*, 112566. [CrossRef]
9. Ye, C.; Liu, X.; Xin, F.; Lu, T.J. Underwater Acoustic Absorption of Composite Anechoic Layers With Inner Holes. *J. Vib. Acoust.* **2019**, *141*, 041006. [CrossRef]
10. Yang, H.; Xiao, Y.; Zhao, H.; Zhong, J.; Wen, J. On wave propagation and attenuation properties of underwater acoustic screens consisting of periodically perforated rubber layers with metal plates. *J. Sound Vib.* **2019**, *444*, 21–34. [CrossRef]
11. Fu, X.; Jin, Z.; Yin, Y.; Liu, B. Sound absorption of a rib-stiffened plate covered by anechoic coatings. *J. Acoust. Soc. Am.* **2015**, *137*, 1551–1556. [CrossRef] [PubMed]
12. Calvo, D.C.; Thangawng, A.L.; Layman, C.N., Jr.; Casalini, R.; Othman, S.F. Underwater sound transmission through arrays of disk cavities in a soft elastic medium. *J. Acoust. Soc. Am.* **2015**, *138*, 2537–2547. [CrossRef] [PubMed]
13. Wen, J.; Zhao, H.; Lv, L.; Yuan, B.; Wang, G.; Wen, X. Effects of locally resonant modes on underwater sound absorption in viscoelastic materials. *J. Acoust. Soc. Am.* **2011**, *130*, 1201–1208. [CrossRef] [PubMed]
14. Jayakumari, V.G.; Shamsudeen, R.K.; Ramesh, R.; Mukundan, T. Modeling and validation of polyurethane based passive underwater acoustic absorber. *J. Acoust. Soc. Am.* **2011**, *130*, 724–730. [CrossRef]
15. Shaid Sujon, M.A.; Islam, A.; Nadimpalli, V.K. Damping and sound absorption properties of polymer matrix composites: A review. *Polym. Test.* **2021**, *104*, 107388. [CrossRef]
16. Zhang, X.; Qu, Z.; Wang, H. Engineering Acoustic Metamaterials for Sound Absorption: From Uniform to Gradient Structures. *iScience* **2020**, *23*, 101110. [CrossRef]
17. Sharma, G.S.; Skvortsov, A.; MacGillivray, I.; Kessissoglou, N. Acoustic performance of periodic steel cylinders embedded in a viscoelastic medium. *J. Sound Vib.* **2019**, *443*, 652–665. [CrossRef]
18. Lee, T.; Iizuka, H. Heavily overdamped resonance structurally engineered in a grating metasurface for ultra-broadband acoustic absorption. *Appl. Phys. Lett.* **2018**, *113*, 101903. [CrossRef]
19. Wang, T.; Wang, G.-B.; Zhang, R.-J.; Ke, M.-Z. Low-frequency underwater sound absorption metamaterial. *Phys. Scr.* **2022**, *97*, 125706. [CrossRef]
20. Arjunan, A.; Baroutaji, A.; Robinson, J. Advances in Acoustic Metamaterials. In *Encyclopedia of Smart Materials*; Elsevier: Amsterdam, The Netherlands, 2022; pp. 1–10.
21. Ivansson, S.M. Markov-chain Monte Carlo identification of favorable design choices with application to anechoic coatings. *J. Acoust. Soc. Am.* **2014**, *135*, 3338–3351. [CrossRef]
22. Ye, C.; Liu, X.; Xin, F.; Lu, T.J. Influence of hole shape on sound absorption of underwater anechoic layers. *J. Sound Vib.* **2018**, *426*, 54–74. [CrossRef]
23. Lane, R. Absorption mechanisms for waterborne sound in Alberich anechoic layers. *Ultrasonics.* **1981**, *19*, 28–30. [CrossRef]
24. Zhao, D.; Zhao, H.; Yang, H.; Wen, J. Optimization and mechanism of acoustic absorption of Alberich coatings on a steel plate in water. *Appl. Acoust.* **2018**, *140*, 183–187. [CrossRef]
25. Gao, N.; Lu, K. An underwater metamaterial for broadband acoustic absorption at low frequency. *Appl. Acoust.* **2020**, *169*, 107500. [CrossRef]
26. Jin, G.; Shi, K.; Ye, T.; Zhou, J.; Yin, Y. Sound absorption behaviors of metamaterials with periodic multi-resonator and voids in water. *Appl. Acoust.* **2020**, *166*, 107351. [CrossRef]
27. Wang, Z.; Huang, Y.; Zhang, X.; Li, L.; Chen, M.; Fang, D. Broadband underwater sound absorbing structure with gradient cavity shaped polyurethane composite array supported by carbon fiber honeycomb. *J. Sound Vib.* **2020**, *479*, 115375. [CrossRef]
28. Zhong, J.; Zhao, H.; Yang, H.; Yin, J.; Wen, J. Effect of Poisson's loss factor of rubbery material on underwater sound absorption of anechoic coatings. *J. Sound Vib.* **2018**, *424*, 293–301. [CrossRef]
29. Shi, K.; Jin, G.; Liu, R.; Ye, T.; Xue, Y. Underwater sound absorption performance of acoustic metamaterials with multilayered locally resonant scatterers. *Results Phys.* **2019**, *12*, 132–142. [CrossRef]
30. Shi, K.; Jin, G.; Ye, T.; Zhang, Y.; Chen, M.; Xue, Y. Underwater sound absorption characteristics of metamaterials with steel plate backing. *Appl. Acoust.* **2019**, *153*, 147–156. [CrossRef]

31. Zhong, J.; Zhao, H.; Yang, H.; Yin, J.; Wen, J. On the accuracy and optimization application of an axisymmetric simplified model for underwater sound absorption of anechoic coatings. *Appl. Acoust.* **2019**, *145*, 104–111. [CrossRef]

32. Meng, T. Simplified model for predicting acoustic performance of an underwater sound absorption coating. *J. Vib. Control.* **2021**, *20*, 339–354. [CrossRef]

33. Yu, C.; Duan, M.; He, W.; Xin, F.; Lu, T.J. Underwater anechoic layer with parallel metallic plate insertions: Theoretical modelling. *J. Micromech. Microeng.* **2021**, *31*, 074002. [CrossRef]

34. Wang, T.; Liu, J.; Chen, M. Underwater sound absorption of a meta-absorption layer with double negativity. *Appl. Acoust.* **2021**, *181*, 108182. [CrossRef]